

Continuous K-space Recovery Network with Image Guidance for Fast MRI Reconstruction

Yucong Meng, Zhiwei Yang, Minghong Duan, Yonghong Shi, Zhijian Song

Abstract—Magnetic resonance imaging (MRI) is a crucial tool for clinical diagnosis while facing the challenge of long scanning time. To reduce the acquisition time, fast MRI reconstruction aims to restore high-quality images from the undersampled k-space. Existing methods typically train deep learning models to map the undersampled data to artifact-free MRI images. However, these studies often overlook the unique properties of k-space and directly apply general networks designed for image processing to k-space recovery, leaving the precise learning of k-space largely underexplored. In this work, we propose a continuous k-space recovery network from a new perspective of implicit neural representation with image domain guidance, which boosts the performance of MRI reconstruction. Specifically, (1) an implicit neural representation based encoder-decoder structure is customized to continuously query unsampled k-values. (2) an image guidance module is designed to mine the semantic information from the low-quality MRI images to further guide the k-space recovery. (3) a multi-stage training strategy is proposed to recover dense k-space progressively. Extensive experiments conducted on CC359, fastMRI, and IXI datasets demonstrate the effectiveness of our method and its superiority over other competitors.

Index Terms—Magnetic resonance imaging (MRI), image reconstruction, implicit neural representation, transformer.

I. INTRODUCTION

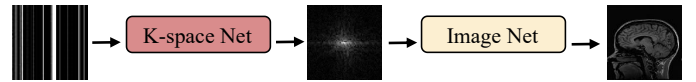
MAGNETIC resonance imaging (MRI) is widely used for clinical diagnosis because of its advantages of no radiation, high resolution, and satisfactory soft-tissue contrast. However, the MRI acquisition process is inherently slow due to both physiological and hardware limitations, as well as the sequential nature of obtaining measurements in the frequency domain (k-space) [1], [2]. The extended scan time required to obtain fully sampled MRI images causes patient discomfort and reduces accessibility to the modality. To speed up this process, accelerated MRI aims to reconstruct MRI images from undersampled k-space [3]–[5]. However, the aliasing artifacts caused by such insufficient sampling often affect the clinical diagnosis. Therefore, it becomes a significant challenge how to reduce the amount of k-space acquisition while maintaining or even improving MRI image quality.

Y.Meng, M.Duan, Y.Shi, and Z.Song are with Digital Medical Research Center, School of Basic Medical Science, Fudan University, Shanghai 200032, China, and also with the Shanghai Key Laboratory of Medical Image Computing and Computer Assisted Intervention, Shanghai 200032, China.

Z.Yang is with Academy of Engineering & Technology, Fudan University, Shanghai 200433, China, and also with the Shanghai Key Laboratory of Medical Image Computing and Computer Assisted Intervention, Shanghai 200032, China.

Corresponding authors: Yonghong Shi, Zhijian Song. (email: yonghong.shi@fudan.edu.cn; zjsong@fudan.edu.cn)

(a) Previous studies reconstruct k-space using general models.



(b) We customize k-space net via INR with image guidance.

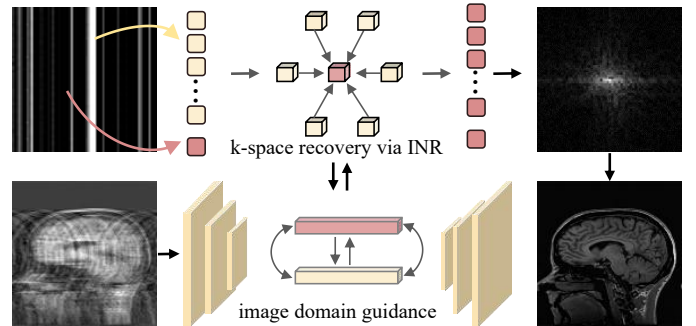


Fig. 1. Our main idea. (a) Previous studies typically employ general networks to reconstruct the undersampled data both in the k-space and image domain. (b) We customize a continuous k-space recovery network from a new perspective of implicit neural representation with image domain guidance, thereby enhancing the performance of MRI reconstruction.

Essentially, the aliasing artifacts arise because undersampling destroys the k-space’s integrity. Many methods ignore the importance of k-space recovery and focus on reconstruction only from low-quality MRI images [6]–[10]. To this end, several works consider recovering k-space via an external network as shown in Fig.1 (a) [11]–[18]. Despite some progress, they neglect the unique properties inherent to the k-space and directly adopt general CNNs which are not suitable for k-space recovery. CNNs have an inductive bias that their kernels are shared across spatial positions. However, in k-space, spatial positions represent frequency components of sine and cosine functions, and identical patterns at different positions can represent entirely different information [19]–[22]. Previous works overlook this specific characteristic of k-space and adopt conventional image processing networks for processing k-space, resulting in inferior results. Hence, designing a customized network for undersampled k-space recovery is the key to reconstructing satisfactory MRI images.

Intuitively, a high-quality MRI image is generated from a continuous k-space where each coordinate has a specific signal. Therefore, the ideal reconstruction of k-space should be modeled as a function where arbitrary coordinates can be mapped into a k-value. Such a concept of continuous representation is consistent with implicit neural representation (INR), which emerged as a new paradigm for image super-resolution [23], [24]. Specifically, INR uses a neural network

to model images as continuous functions of spatial coordinates instead of discrete pixel grids. The network takes spatial coordinates as input and predicts corresponding pixel values. After training on low-resolution data, the model generates high-resolution images by querying dense coordinates, preserving fine details and enabling arbitrary resolution output [23], [25].

Inspired by this, we propose to boost the performance of MRI reconstruction by recovering complete k-space via implicit neural representation. However, simply introducing INR to MRI reconstruction still faces several challenges. (1) INR originates from the processing of natural images, where rich semantic information is provided. Compared to it, the k-space spectrum exhibits a simple structure, making such continuous recovery challenging. Therefore, more information needed to be provided to guide k-space reconstruction. (2) The practice of accelerated scanning leads to excessively sparse sampled points, directly recovering a dense k-space from such sparsely sampled points inevitably introduces over-smoothing and distortion. A more gentle recovery paradigm should be designed to progressively reconstruct the dense k-space.

Based on these, we propose an Image-domain Guided K-space Recovery Network, named IGKR-Net. As shown in Fig.1 (b), we customize a k-space network from a new perspective of INR with image guidance for MRI reconstruction.

Specifically, (1) We propose an INR-based encoder-decoder structure, directly processing signals in the k-space domain. To detail, we design an encoder based on the standard transformer including multi-head self-attention (MSA) and feed-forward network (FFN), to encode the sampled k-values and their corresponding coordinates. Thus, a continuous feature representation of the k-space spectrum is learned. Subsequently, we adopt standard transformer decoder layers consisting of multi-head cross-attention (MCA), MSA, and FFN, to dynamically query the unsampled k-values using their coordinates and thus reconstruct the k-space spectrum with high quality. (2) We design an image domain guidance module to mine semantic information from the undersampled MRI images and guide the above k-space recovery. (3) We propose a tri-attention refinement module to further provide more details in the image domain. (4) To mitigate the issues of over-smoothing and distortion caused by directly recovering dense k-space from sparsely sampled points, we introduce a multi-stage training strategy to obtain finer reconstruction results step-by-step.

Overall, the main contributions of our work are as follows:

- An INR based encoder-decoder structure is proposed to directly process signals in the k-space. Benefiting from this structure, our work can reconstruct the high-quality k-space.
- An image domain guidance module is designed to mine the information from undersampled MRI images and guide the k-space recovery. Thanks to the design of this, we provide rich semantic information for the challenging k-space recovery.
- A multi-stage training strategy is introduced to progressively reconstruct MRI images from low resolution to high resolution. Thanks to this paradigm, we mitigate concerns of over-smoothing and distortion and obtain precise results.
- Extensive experiments are conducted on three public datasets, CC359, fastMRI, and IXI, demonstrating the superiority of our method over previous reconstruction approaches.

II. RELATED WORK

A. Deep Learning for Accelerated MRI

Traditional MRI techniques involve the acquisition of dense k-space data, resulting in extended scan time. In recent years, a variety of deep neural networks have been explored for accelerated MRI. The pipeline for these methods usually consists of three steps, i.e., roughly recovering the complete k-space from undersampled data by employing a zero-filling strategy, then generating low-quality MRI images via inverse fast Fourier transform (IFFT), and finally learning the mapping relationship between such low-quality MRI images and their corresponding high-quality ones by adapting advanced CNN architectures, including UNet [26], deep residual network [27], generative adversarial network [28], and deep cascaded network [29].

Besides, benefiting from the capability of learning global information, transformers [30]–[33] have recently achieved satisfactory performance for accelerated MRI. Feng et al. [34], [35] pioneered the introduction of the transformer in the field of MRI reconstruction, integrating MRI reconstruction with super-resolution in a multitask fashion. Huang et al. [36] proposed a parallel imaging coupled swin transformer-based model. To sum up, the data-driven nature of deep learning allows these methods to learn the mapping between low-quality input and artifact-free images. However, such networks operate only in the image domain, making it challenging to ensure the consistency of the k-space.

To this end, several attempts have been made to incorporate physics information in this line of work, including enforcing k-space consistency directly after image enhancement or adding k-space consistency as an additional cost function term during training. For example, Hyun et al. [11] enhanced k-space consistency by directly replacing the generated k-values with the corresponding original ones. Yang et al. [12] considered incorporating an additional k-space consistency term into the loss function. Though effective at reducing artifacts, they fundamentally only focus on image-domain restoration, with k-space information used for coarse correction or consistency supervision. The images relied upon by such methods are severely compromised, and this damage is irreversible [37], [38]. Indeed, the continuity of the k-space is crucial for the recovery of high-quality MRI images. However, these approaches neglect this and result in inferior results.

B. K-space Recovery

Recently, some studies began to recover k-space. Taejoon Eo et al. [39] proposed KIKINet, using a combination of 4 different CNNs to operate on k-space, image, k-space, and image sequentially. Osvald Nitski et al. [40] proposed CDF-Net, using two UNet to operate on the image and k-space domain respectively, and combining them into an end-to-end framework. Wang et al. [41] introduced a compressed sensing equivariant imaging prior framework that combines a data preparation strategy for generalizable MRI reconstruction. Zhao et al. [42] proposed SwinGAN, consisting of a k-space generator and an image-domain generator that utilizes swin transformer as the backbone. Such approaches aimed to preserve and leverage the k-space information, achieving more

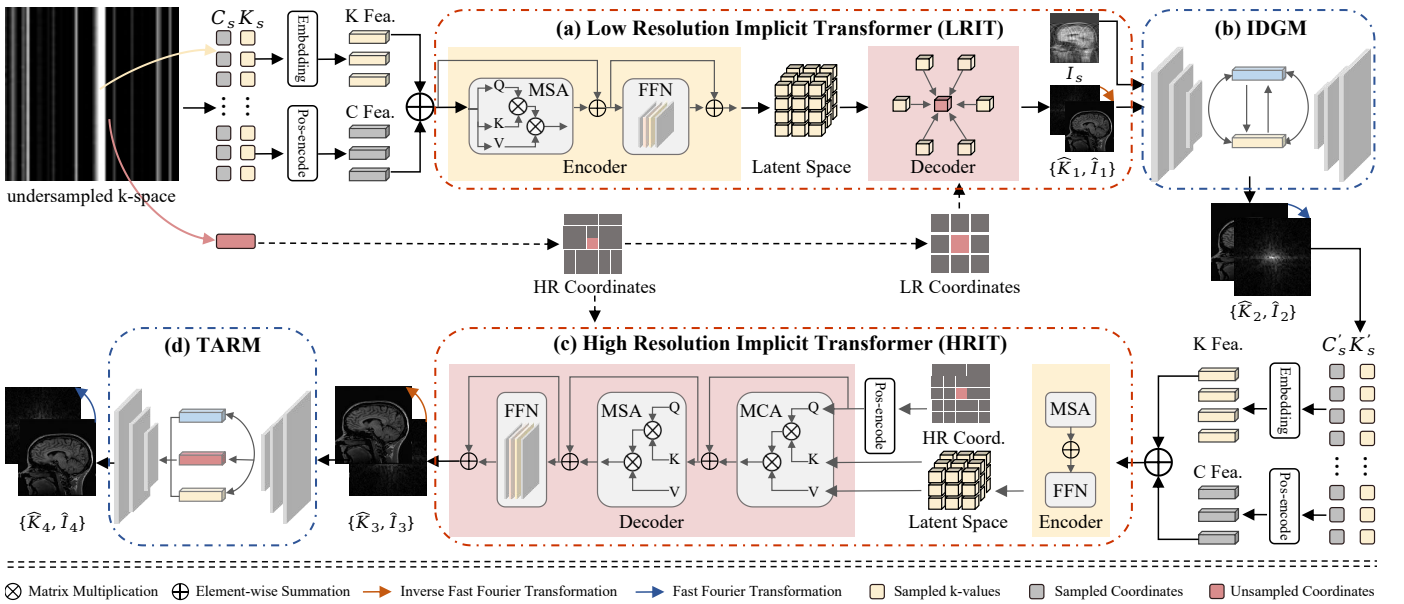


Fig. 2. The overall architecture of the proposed IGKR Net. Given the undersampled k-space, we first encode the coordinates and k-values of the sampled points, and the resulting features are added and then fed into LRIT. In LRIT, we use the LR coordinates to query and get the recovered results, i.e., \hat{K}_1 and \hat{I}_1 . Next, we send \hat{I}_1 into IDGM and get \hat{K}_2 and \hat{I}_2 with the guidance of the low-quality image I_s . Then, the k-values and coordinates of \hat{K}_2 are encoded and fed into HRIT, where \hat{K}_3 and \hat{I}_3 are obtained by querying HR coordinates. Finally, we design TARM to refine \hat{I}_3 , yielding the final output \hat{K}_4 and \hat{I}_4 .

accurate results. However, they all treated the k-space spectrums as natural images, directly employing general networks for feature extraction and spectrum reconstruction.

Besides, in k-space based parallel imaging reconstruction, some methods such as GRAPPA [43], SPIRiT [44] and AC-LORAKS [45] used linear convolution to interpolate undersampled k-space data. They assumed that the k-space data has a shifted autoregressive structure and learned the scan-specific autoregressive relationships required to recover missing sample scans from the fully sampled auto-calibration (ACS) data. However, at high acceleration, these methods produce inherent noise amplification and degrade image quality. Recently, the structure of the linear GRAPPA method has been transformed into a nonlinear deep learning method called RAKI [46]. RAKI performs scan-specific k-space interpolation using CNNs trained on the ACS data, and provides an improvement in both image quality and noise reduction over traditional PI methods that use linear k-space interpolation. However, the availability of training databases with different scans and their interpretability hinders its adaptability.

C. Implicit Neural Representation

Recently, implicit neural representation (INR) has been proposed as a method of continuous representation for various tasks [47]–[52]. INR employs neural networks, typically coordinate-based multilayer perceptrons (MLPs), to establish mapping relationships between coordinates and their corresponding signal values [53], [54].

Because of its continuous and precise representation, INR has been applied to various tasks of image enhancement [23], [24]. For example, LIIF [23] proposed a new framework for arbitrary-scale super-resolution using INR. Li et al. [25] proposed a novel adaptive local image function (A-LIIF) to

alleviate structural distortions and ringing artifacts around edges. Motivated by the feature interpolation in LIIF, Wu et al. [55] designed an INR-based network for achieving 3D MRI super-resolution at arbitrary scales. In summary, 2D INR models an image as a continuous function using latent space interpolation, enabling precise querying of signal intensity for any given coordinates. This concept provides a novel approach for achieving high-quality recovery in k-space.

III. METHODOLOGY

A. Preliminary

1) *MRI Reconstruction*: Let K represent the complex-valued, fully sampled k-space acquired from the MRI scanner, accelerated MRI usually employs undersampling to acquire a reduced set of k-space, i.e., K_s , while a substantial portion of the k-space, i.e., K_{us} , is unsampled. Here, we simulate this undersampling process by the element-wise multiplication (\otimes) of K with a two-dimensional mask M :

$$K_s = M \otimes K, K_{us} = (1 - M) \otimes K \quad (1)$$

Correspondingly, low-quality MRI image I_s can be obtained, i.e., $I_s = IFFT(K_s)$. To recover high-quality MRI image \hat{I} , deep learning methods typically leverage extensive training data to establish a mapping relationship between \hat{I} and the sampled data (I_s, K_s) , which can be formulated as:

$$\hat{I} = f_{\theta}(I_s, K_s) \quad (2)$$

Here, θ is the parameters set of the deep neural network. In contrast to these methods, our IGKR-Net focuses on recovering K_{us} , which is the fundamental cause of MRI image blurring and is crucial for high-quality MRI reconstruction.

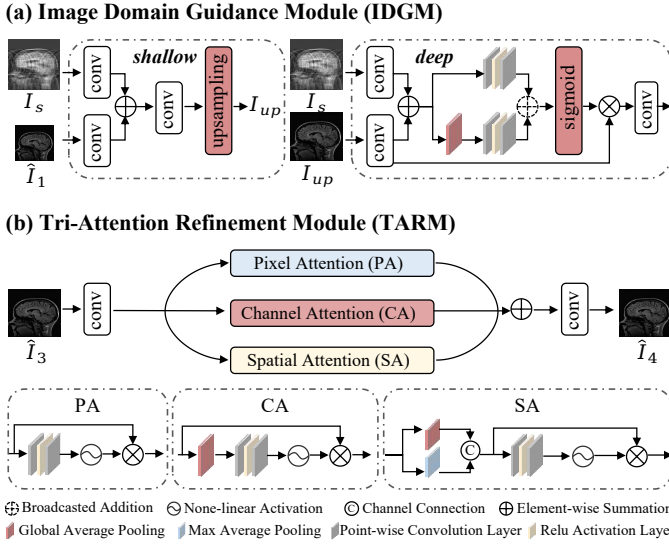


Fig. 3. (a) The proposed IDGM consists of two stages, i.e., shallow fusion stage and deep fusion stage. (b) The proposed TARM consists of three branches, i.e., PA, CA, and SA.

2) *Implicit Neural Representation*: In contrast to the typical representation of images using discrete pixel arrays, implicit neural representation (INR) models the mapping relationship between image coordinates C and their corresponding intensity values i as a function, which can be formulated as:

$$i = f_{\theta}(C, V_c) \quad (3)$$

Here, V_c represents the feature vector specific to the pixel at spatial coordinates C and is obtained by establishing a latent space by training an encoder. Function f_{θ} is fitted using a multilayer perceptron (MLP) and is continuous to the spatial coordinate system. Therefore, once f_{θ} is well-fitted, intensity values can be queried at arbitrary coordinates, thereby achieving a continuous visual representation of the image.

3) *continuous K-space Recovery Network via INR*: As described in (1), it is common to undersample the k-space for accelerated MRI. The correct recovery of the unsampled k-values, i.e., K_{us} , is crucial for high-quality MRI reconstruction. Drawing inspiration from the continuous image modeling of INR, we customize a k-space recovery net. Specifically, K_{us} can be queried by using their coordinates C_{us} :

$$K_{us} = f_{\theta}(C_{us}, V_{C_{us}}) \quad (4)$$

Where the latent feature vectors $V_{C_{us}}$ are obtained by encoding the sampled k-values K_s and their coordinates C_s using a designed encoder Φ_{Enc} . The function f_{θ} is fitted through training a decoder Φ_{Dec} , which can be formulated as:

$$K_{us} = \Phi_{Dec}(C_{us}, \Phi_{Enc}(K_s, C_s)) \quad (5)$$

Here, the encoder Φ_{Enc} and decoder Φ_{Dec} are implemented through the transformer attention mechanism.

B. Network Architecture

As shown in Fig.2, the overall architecture of our IGKR-Net can be roughly divided into two parts, i.e., the primary part directly processing in k-space domain (denoted as red lines), and the auxiliary part operating on the data of image domain

(denoted as blue lines). The k-space part comprises two modules, i.e., LRIT and HRIT, to reconstruct the k-space from low resolution (LR) to high resolution (HR) progressively, while the image part comprises IDGM and TRAM for image-domain guidance and final refinement, respectively.

Specifically, given undersampled k-space $K \in R^{2 \times H \times W}$ as input, we obtain the set of k-values K_s and the corresponding coordinates C_s , from the sampled points. Then, K_s and C_s are encoded separately, and the resulting features are summed to form a vector sequence which is used as the input of LRIT. LRIT first uses a transformer-based encoder to learn a latent space and then recover a complete while LR k-space \hat{K}_1 by querying pre-designed LR coordinates through the decoder. Subsequently, we get \hat{I}_1 through IFFT and send it into IDGM to deeply mine semantic information from the corrupted image I_s and guide the k-space recovery. We fuse I_s with \hat{I}_1 , obtaining \hat{I}_2 and \hat{K}_2 . Next, HRIT uses the recovered dense \hat{K}_2 to further establish a continuous latent space, recovering complete and HR \hat{K}_3 and its corresponding \hat{I}_3 using the HR coordinates. Finally, we design TARM to refine \hat{I}_3 in the image domain, resulting in the final output, i.e., \hat{I}_4 and \hat{K}_4 .

Besides, to mitigate issues of over-smoothing and distortion and obtain satisfactory results progressively, a multi-stage training strategy is proposed. Below we first present the design of LRIT, IDGM, HRIT, and TARM, respectively, followed by a description of the training strategy.

1) *Low Resolution Implicit Transformer (LRIT)*: LRIT and HRIT share the same structure but differ in their inputs. Here, we take LRIT as an example to explain its structure in detail. As depicted in Fig.2 (a), LRIT is an encoder-decoder architecture aiming to recover LR k-space \hat{K}_1 and its corresponding \hat{I}_1 by querying the LR coordinates.

Specifically, given a set of sampled k-values K_s and its coordinates C_s , a tokenization procedure is firstly applied to convert them into a vector sequence \mathcal{V} :

$$\mathcal{V} = MLP(K_s) + PE(C_s) \quad (6)$$

where a multilayer perceptrons (MLPs) layer is applied to K_s , and PE refers to positional encodings with sine and cosine functions. Then we send \mathcal{V} into the encoder of LRIT which consists of multi-head self-attention (MSA) and feed-forward network (FFN) to obtain the latent space \mathcal{S} as follows:

$$\mathcal{S} = FFN(MSA(\mathcal{V})) \quad (7)$$

Subsequently, we design a decoder that employs standard transformer decoder layers consisting of multi-head cross attention (MCA), MSA, and FFN, to recover complete while low-resolution k-space, i.e., \hat{K}_1 . In detail, for MCA, we employ encoded LR coordinates $C_{lr} \in R^{\frac{H}{2} \times \frac{W}{2}}$ to serve as the query (Q) and apply two different linear projects to latent space \mathcal{S} to serve as the key (K) and value (V). After that, we apply MSA to the weighted feature again and decode it via FFN. Thus, we obtain a low-resolution while complete k-space $\hat{K}_1 \in R^{2 \times \frac{H}{2} \times \frac{W}{2}}$, as well as its corresponding MRI image $\hat{I}_1 \in R^{1 \times \frac{H}{2} \times \frac{W}{2}}$. Which can be formulated as:

$$\hat{K}_1 = FFN(MSA(MCA(Q, K, V))) \quad (8)$$

$$\hat{I}_1 = IFFT(\hat{K}_1) \quad (9)$$

2) *Image Domain Guidance Module (IDGM)*: As shown in Fig.2 (b), our IDGM fuses the low-quality image I_s and the output of LRIT, i.e., \hat{I}_1 , to fully utilize the original image information and guide the process of k-space recovery.

Fig.3 (a) illustrates the detailed structure of the IDGM, which can be divided into two stages: shallow stage and deep stage. Specifically, during the shallow stage, we firstly perform two convolutions with different strides to extract shallow features from I_s and \hat{I}_1 and unify them to the same size, i.e., $\hat{I}_1 \in R^{1 \times \frac{H}{2} \times \frac{W}{2}} \rightarrow R^{h \times \frac{H}{2} \times \frac{W}{2}}$, $I_s \in R^{1 \times H \times W} \rightarrow R^{h \times \frac{H}{2} \times \frac{W}{2}}$, where h denotes the channel number. Subsequently, the features are fused via element-wise summation and restored to $I_{up} \in R^{1 \times H \times W}$ via another convolution and upsampling $up(\cdot)$, i.e., $I_{up} = up(conv(conv(\hat{I}_1) + conv(I_s)))$.

During the deep fusion, we first employ two convolution heads to extract image-specific shallow features from I_s and I_{up} , respectively. After element-wise summation, the fused feature is sent into two attention branches, generating local channel attention A_l without any pooling and global channel attention A_g by using global average pooling, respectively. Given A_l and A_g , the final attention weights A can be obtained by the broadcasted addition (+), i.e., $A = sigmoid(A_l + A_g)$. Finally, we obtain \hat{I}_2 , as well as its corresponding k-space \hat{K}_2 :

$$\hat{I}_2 = conv(A \otimes conv(I_{up})) \quad (10)$$

$$\hat{K}_2 = FFT(\hat{I}_2) \quad (11)$$

3) *High Resolution Implicit Transformer (HRIT)*: As shown in Fig.2 (c), to further reconstruct the dense k-space with high resolution, we apply the implicit transformer again. Different from the above LRIT, here we use the K'_s and C'_s from restored \hat{K}_2 to form vector sequence \mathcal{V}' , i.e., $\mathcal{V}' = MLP(K'_s) + PE(C'_s)$. Then we get latent space \mathcal{S}' :

$$\mathcal{S}' = FFN(MSA(\mathcal{V}')) \quad (12)$$

Finally, we obtain the high quality k-space \hat{K}_3 and its corresponding MRI image \hat{I}_3 by encoding HR coordinates $C_{hr} \in R^{H \times W}$ as query (Q') and projecting \mathcal{S}' as key (K') and value (V'). Which can be formulated as:

$$\hat{K}_3 = FFN(MSA(MCA(Q', K', V'))) \quad (13)$$

$$\hat{I}_3 = IFFT(\hat{K}_3) \quad (14)$$

4) *Tri-Attention Refinement Module (TARM)*: As shown in Fig.2 (d), our TARM further refines the reconstruction result \hat{I}_3 in the image domain, providing it with richer image details.

Fig.3 (b) illustrates the detailed structure of the TARM, which comprises a convolution head and three attention branches, i.e., spatial attention (SA), channel attention (CA), and pixel attention (PA). Specifically, for an image that needs to be refined, i.e., \hat{I}_3 , the TARM firstly extracts shallow feature f by a convolution. Then, f is sent into three attention branches. To detail, PA generates a 3D attention mask M_1 without any pooling or sampling, which means the output features have local information. CA uses global average pooling (GAP) to generate the 1D attention mask, i.e., M_2 , to obtain features that have global information. SA uses GAP or max average pooling (MAP) to generate a 2D attention mask, i.e., M_3 , to get features with global information. Finally,

Algorithm 1: Training procedure

```

stage_1: Train LRIT;
for each epoch  $\in [E_0, E_1]$  do
    Get ( $K_s, C_s, C_{lr}, K_{lr}, I_{lr}$ );
    Train LRIT by minimizing
     $L_{stage\_1} = L_1$ 
end
stage_2: Joint optimization of LRIT and DIFM;
for each epoch  $\in [E_1, E_2]$  do
    Get ( $K_s, C_s, C_{lr}, K_{lr}, I_{lr}, I_s, K, I$ );
    Train LRIT and DIFM by minimizing
     $L_{stage\_2} = L_1 + L_2$ 
end
stage_3: Joint optimization of LRIT, DIFM, and HRIT;
for each epoch  $\in [E_2, E_3]$  do
    Get ( $K_s, C_s, C_{lr}, K_{lr}, I_{lr}, I_s, K, I, C_{us}$ );
    Train LRIT, DIFM, and HRIT by minimizing
     $L_{stage\_3} = L_1 + L_2 + L_3$ 
end
stage_4: Joint optimization of LRIT, DIFM, HRIT, and TARM;
for each epoch  $\in [E_3, E_4]$  do
    Get ( $K_s, C_s, C_{lr}, K_{lr}, I_{lr}, I_s, K, I, C_{us}$ );
    Train LRIT, DIFM, HRIT, TARM by minimizing
     $L_{stage\_4} = L_1 + L_2 + L_3 + L_4$ 
end
    
```

the weighted features from three attention branches are fused via element-wise summation, to obtain the final reconstruction results \hat{I}_4 and its corresponding k-space \hat{K}_4 :

$$\hat{I}_4 = conv(M_1 \otimes f + M_2 \otimes f + M_3 \otimes f) \quad (15)$$

$$\hat{K}_4 = FFT(\hat{I}_4) \quad (16)$$

5) *Loss Functions and Training Strategy*: Following [42], [60], we evaluate the intermediate outputs of various modules by using the L_2 loss, which consists of two terms. To detail, the first term is used to constrain the consistency between the reconstructed k-space \hat{K}_i and corresponding fully sampled k-space, i.e., K_{lr} or K , while the second term is used to constrain the consistency between the reconstructed image \hat{I}_i and the corresponding fully sampled image, i.e., I_{lr} or I :

$$L_i = \begin{cases} \|K_{lr} - \hat{K}_i\|_2 + \|I_{lr} - \hat{I}_i\|_2 & \text{if } i = 1 \\ \|K - \hat{K}_i\|_2 + \|I - \hat{I}_i\|_2 & \text{if } i = 2, 3, 4 \end{cases} \quad (17)$$

where I , I_{lr} , and K_{lr} is obtained via $I = IFFT(K)$, $I_{lr} = downsample(I)$, and $k_{lr} = FFT(I_{lr})$, respectively. Furthermore, to mitigate the issues of over-smoothing and distortion and obtain finer reconstruction results step-by-step, we design a multi-stage training strategy, as illustrated by Algorithm 1. Specifically, we divide the training process into four stages, i.e., $stage = stage_i$, when $epoch \in [E_{i-1}, E_i] \Big|_{i=1}^4$. In summary, our IGIT-Net recovers the precise MRI images progressively by optimizing the loss at various stages:

$$L_{stage_j} = \sum_{i=1}^j L_i \quad (18)$$

TABLE I
QUANTITATIVE RESULTS OF THE COMPARISON EXPERIMENTS ON THE CC359 VALIDATION DATASET USING DIFFERENT MASKS. A HIGHER VALUE OF METRIC \uparrow INDICATES BETTER PERFORMANCE, WHEREAS A LOWER VALUE OF METRIC \downarrow CORRESPONDS TO IMPROVED PERFORMANCE.

Method	1D Cartesian mask, sampling ratio = 20%				1D Cartesian mask, sampling ratio = 40%			
	PSNR \uparrow	SSIM \uparrow	NMSE \downarrow	LPIPS \downarrow	PSNR \uparrow	SSIM \uparrow	NMSE \downarrow	LPIPS \downarrow
ZF	21.62 \pm 2.80	0.6254 \pm 0.11	0.0936 \pm 0.03	0.3596 \pm 0.04	22.74 \pm 2.83	0.6784 \pm 0.08	0.0723 \pm 0.02	0.2969 \pm 0.04
ResNet [56]	28.13 \pm 3.84	0.8559 \pm 0.14	0.0200 \pm 0.01	0.0858 \pm 0.07	30.05 \pm 3.58	0.9052 \pm 0.07	0.0131 \pm 0.01	0.0569 \pm 0.04
UNet [26]	29.34 \pm 4.59	0.8756 \pm 0.11	0.0156 \pm 0.01	0.0618 \pm 0.05	31.73 \pm 4.70	0.9189 \pm 0.07	0.0090 \pm 0.00	0.0408 \pm 0.04
SwinMR [36]	31.11 \pm 3.87	0.9006 \pm 0.09	0.0124 \pm 0.00	0.0413 \pm 0.03	35.67 \pm 4.13	0.9543 \pm 0.04	0.0045 \pm 0.00	0.0184 \pm 0.02
RefineGAN [57]	29.96 \pm 4.59	0.8888 \pm 0.07	0.0303 \pm 0.02	0.0395 \pm 0.04	38.57 \pm 5.16	0.9656 \pm 0.02	0.0058 \pm 0.01	0.0077 \pm 0.01
SwinGAN [58]	31.32 \pm 3.20	0.9017 \pm 0.06	0.0087 \pm 0.01	0.0390 \pm 0.02	38.67 \pm 4.56	0.9688 \pm 0.02	0.0043 \pm 0.01	0.0156 \pm 0.02
OCUCFormer [59]	32.54 \pm 2.56	0.9166 \pm 0.06	0.0074 \pm 0.02	0.0377 \pm 0.03	38.70 \pm 5.33	0.9690 \pm 0.03	0.0035 \pm 0.02	0.0150 \pm 0.01
Ours	33.06\pm5.27	0.9234\pm0.10	0.0069\pm0.00	0.0362\pm0.04	38.78\pm5.67	0.9703\pm0.05	0.0020\pm0.00	0.0143\pm0.03
Method	2D Gaussian mask, sampling ratio = 20%				2D Gaussian mask, sampling ratio = 40%			
	PSNR \uparrow	SSIM \uparrow	NMSE \downarrow	LPIPS \downarrow	PSNR \uparrow	SSIM \uparrow	NMSE \downarrow	LPIPS \downarrow
ZF	24.23 \pm 3.18	0.5942 \pm 0.10	0.0497 \pm 0.02	0.3796 \pm 0.06	27.22 \pm 3.39	0.6901 \pm 0.07	0.0246 \pm 0.01	0.2543 \pm 0.08
ResNet [56]	28.83 \pm 3.47	0.8576 \pm 0.12	0.0185 \pm 0.02	0.0841 \pm 0.08	31.00 \pm 3.66	0.9102 \pm 0.09	0.0181 \pm 0.05	0.0592 \pm 0.10
UNet [26]	30.39 \pm 4.78	0.8790 \pm 0.12	0.0124 \pm 0.00	0.0578 \pm 0.05	33.39 \pm 4.98	0.9280 \pm 0.08	0.0063 \pm 0.00	0.0362 \pm 0.03
SwinMR [36]	31.44 \pm 4.01	0.8943 \pm 0.09	0.0116 \pm 0.04	0.0441 \pm 0.03	34.36 \pm 3.85	0.9378 \pm 0.05	0.0059 \pm 0.00	0.0220 \pm 0.01
RefineGAN [57]	30.08 \pm 4.61	0.8770 \pm 0.07	0.0303 \pm 0.02	0.0395 \pm 0.03	35.73 \pm 5.05	0.9486 \pm 0.03	0.0098 \pm 0.01	0.0140 \pm 0.01
SwinGAN [58]	34.56 \pm 3.56	0.9233 \pm 0.04	0.0078 \pm 0.01	0.0221 \pm 0.02	38.89 \pm 4.32	0.9676 \pm 0.04	0.0046 \pm 0.02	0.0089 \pm 0.01
OCUCFormer [59]	35.55 \pm 3.20	0.9320 \pm 0.03	0.0050 \pm 0.02	0.0199 \pm 0.01	40.41 \pm 3.89	0.9770 \pm 0.04	0.0027 \pm 0.01	0.0059 \pm 0.01
Ours	37.09\pm5.54	0.9512\pm0.09	0.0029\pm0.00	0.0184\pm0.03	43.04\pm5.72	0.9807\pm0.05	0.0008\pm0.00	0.0048\pm0.01

TABLE II
QUANTITATIVE RESULTS OF THE COMPARISON EXPERIMENTS ON THE FASTMRI VALIDATION DATASET USING DIFFERENT MASKS. A HIGHER VALUE OF METRIC \uparrow INDICATES BETTER PERFORMANCE, WHEREAS A LOWER VALUE OF METRIC \downarrow CORRESPONDS TO IMPROVED PERFORMANCE.

Method	1D Cartesian mask, sampling ratio = 20%				1D Cartesian mask, sampling ratio = 40%			
	PSNR \uparrow	SSIM \uparrow	NMSE \downarrow	LPIPS \downarrow	PSNR \uparrow	SSIM \uparrow	NMSE \downarrow	LPIPS \downarrow
ZF	21.96 \pm 2.19	0.5022 \pm 0.07	0.0818 \pm 0.03	0.4237 \pm 0.06	23.04 \pm 2.28	0.6011 \pm 0.06	0.0638 \pm 0.02	0.3444 \pm 0.06
ResNet [56]	24.54 \pm 2.02	0.6062 \pm 0.09	0.0461 \pm 0.02	0.2469 \pm 0.08	25.75 \pm 2.04	0.7059 \pm 0.07	0.0351 \pm 0.02	0.1791 \pm 0.06
UNet [26]	26.53 \pm 2.22	0.6599 \pm 0.10	0.0316 \pm 0.02	0.2242 \pm 0.08	28.21 \pm 2.33	0.7559 \pm 0.07	0.0220 \pm 0.02	0.1541 \pm 0.06
SwinMR [36]	24.67 \pm 2.21	0.6214 \pm 0.10	0.0480 \pm 0.03	0.2166 \pm 0.06	27.33 \pm 2.46	0.7530 \pm 0.08	0.0271 \pm 0.02	0.1354 \pm 0.05
RefineGAN [57]	25.71 \pm 2.56	0.6961 \pm 0.06	0.0335 \pm 0.02	0.1922 \pm 0.04	29.38 \pm 2.37	0.8054 \pm 0.02	0.0174 \pm 0.08	0.1376 \pm 0.01
SwinGAN [58]	26.60 \pm 2.09	0.7001 \pm 0.08	0.0330 \pm 0.01	0.1996 \pm 0.03	29.89 \pm 2.33	0.8069 \pm 0.06	0.0169 \pm 0.07	0.1225 \pm 0.04
OCUCFormer [59]	27.30 \pm 2.05	0.6998 \pm 0.05	0.0289 \pm 0.01	0.1988 \pm 0.04	29.98 \pm 2.23	0.8072 \pm 0.05	0.0161 \pm 0.03	0.1198 \pm 0.03
Ours	27.67\pm2.52	0.7011\pm0.11	0.0266\pm0.02	0.1843\pm0.07	30.07\pm2.87	0.8073\pm0.08	0.0152\pm0.07	0.1128\pm0.05
Method	2D Gaussian mask, sampling ratio = 20%				2D Gaussian mask, sampling ratio = 40%			
	PSNR \uparrow	SSIM \uparrow	NMSE \downarrow	LPIPS \downarrow	PSNR \uparrow	SSIM \uparrow	NMSE \downarrow	LPIPS \downarrow
ZF	24.84 \pm 1.99	0.5840 \pm 0.07	0.0438 \pm 0.02	0.3364 \pm 0.06	27.57 \pm 2.03	0.7232 \pm 0.05	0.0242 \pm 0.02	0.1985 \pm 0.05
ResNet [56]	26.60 \pm 2.09	0.6611 \pm 0.10	0.0305 \pm 0.02	0.2097 \pm 0.06	27.91 \pm 2.04	0.7600 \pm 0.07	0.0227 \pm 0.01	0.1176 \pm 0.04
UNet [26]	28.10 \pm 2.47	0.6875 \pm 0.11	0.0236 \pm 0.02	0.2058 \pm 0.06	30.20 \pm 2.71	0.7869 \pm 0.07	0.0155 \pm 0.01	0.1094 \pm 0.04
SwinMR [36]	27.42 \pm 2.55	0.6813 \pm 0.11	0.0278 \pm 0.02	0.1994 \pm 0.05	29.54 \pm 2.68	0.7802 \pm 0.07	0.0179 \pm 0.01	0.0988 \pm 0.03
RefineGAN [57]	28.29 \pm 2.53	0.7766 \pm 0.06	0.0211 \pm 0.01	0.1533 \pm 0.03	31.52 \pm 2.41	0.8253 \pm 0.03	0.0150 \pm 0.01	0.0681 \pm 0.02
SwinGAN [58]	29.22 \pm 2.34	0.7455 \pm 0.10	0.0200 \pm 0.01	0.1502 \pm 0.04	31.89 \pm 2.44	0.8277 \pm 0.04	0.0144 \pm 0.02	0.0677 \pm 0.02
OCUCFormer [59]	29.70 \pm 2.55	0.7489 \pm 0.06	0.0198 \pm 0.02	0.1500 \pm 0.03	32.00 \pm 2.23	0.8288 \pm 0.03	0.0166 \pm 0.01	0.0676 \pm 0.02
Ours	29.84\pm3.18	0.7500\pm0.11	0.0188\pm0.02	0.1497\pm0.06	32.07\pm3.65	0.8394\pm0.07	0.0124\pm0.01	0.0670\pm0.03

IV. EXPERIMENTS

A. Implementation Details

1) *Datasets*: We use two real k-space datasets, CC359 and fastMRI, and one simulated dataset, IXI, as described below.

CC359 dataset The public brain MR raw data set—the Calgary-Campinas dataset, which comes from a clinical MR

scanner (Discovery MR750; GE Healthcare, Waukesha, WI, USA)—is used to train and test our proposed model. In total, 4129 slices from 25 volumes are randomly selected to form the training set, and the testing set is composed of 1650 slices from 10 other volumes.

fastMRI dataset The fastMRI dataset is currently the

TABLE III
 QUANTITATIVE RESULTS OF THE COMPARISON EXPERIMENTS ON THE IXI TEST DATASET USING DIFFERENT MASKS. A HIGHER VALUE OF METRIC \uparrow INDICATES BETTER PERFORMANCE, WHEREAS A LOWER VALUE OF METRIC \downarrow CORRESPONDS TO IMPROVED PERFORMANCE.

Method	1D Cartesian mask, sampling ratio = 20%				1D Cartesian mask, sampling ratio = 40%			
	PSNR \uparrow	SSIM \uparrow	NMSE \downarrow	LPIPS \downarrow	PSNR \uparrow	SSIM \uparrow	NMSE \downarrow	LPIPS \downarrow
ZF	22.57 \pm 2.42	0.6994 \pm 0.07	0.1406 \pm 0.03	0.3158 \pm 0.04	23.81 \pm 2.46	0.7443 \pm 0.06	0.1058 \pm 0.03	0.2509 \pm 0.04
ResNet [56]	29.23 \pm 3.18	0.9249 \pm 0.04	0.0323 \pm 0.01	0.0416 \pm 0.02	32.69 \pm 3.27	0.9609 \pm 0.02	0.0148 \pm 0.01	0.0229 \pm 0.01
UNet [26]	30.54 \pm 3.43	0.9434 \pm 0.03	0.0244 \pm 0.01	0.0291 \pm 0.01	33.72 \pm 3.53	0.9685 \pm 0.02	0.0119 \pm 0.01	0.0159 \pm 0.01
SwinMR [36]	34.15 \pm 3.51	0.9652 \pm 0.02	0.0123 \pm 0.01	0.0133 \pm 0.01	37.70 \pm 3.57	0.9805 \pm 0.01	0.0055 \pm 0.00	0.0055 \pm 0.01
RefineGAN [57]	32.96 \pm 2.58	0.9500 \pm 0.01	0.0126 \pm 0.01	0.0142 \pm 0.01	40.33 \pm 3.22	0.9788 \pm 0.02	0.0039 \pm 0.01	0.0028 \pm 0.01
SwinGAN [58]	33.53 \pm 3.32	0.9633 \pm 0.02	0.0120 \pm 0.01	0.0145 \pm 0.01	41.42 \pm 3.43	0.9891 \pm 0.01	0.0031 \pm 0.00	0.0022 \pm 0.00
OCUCFormer [59]	33.97 \pm 3.54	0.9676 \pm 0.02	0.0119 \pm 0.01	0.0138 \pm 0.02	41.26 \pm 3.88	0.9897 \pm 0.01	0.0028 \pm 0.01	0.0020\pm0.01
Ours	34.40\pm3.98	0.9710\pm0.02	0.0113\pm0.01	0.0132\pm0.01	41.48\pm4.09	0.9924\pm0.01	0.0023\pm0.00	0.0033 \pm 0.00

Method	2D Gaussian mask, sampling ratio = 20%				2D Gaussian mask, sampling ratio = 40%			
	PSNR \uparrow	SSIM \uparrow	NMSE \downarrow	LPIPS \downarrow	PSNR \uparrow	SSIM \uparrow	NMSE \downarrow	LPIPS \downarrow
ZF	24.49 \pm 3.02	0.6020 \pm 0.09	0.0924 \pm 0.02	0.3774 \pm 0.05	27.76 \pm 3.01	0.6968 \pm 0.07	0.0436 \pm 0.01	0.2617 \pm 0.05
ResNet [56]	31.47 \pm 3.65	0.9446 \pm 0.03	0.0199 \pm 0.01	0.0326 \pm 0.02	34.98 \pm 3.58	0.9715 \pm 0.02	0.0088 \pm 0.00	0.0183 \pm 0.02
UNet [26]	33.19 \pm 4.07	0.9608 \pm 0.03	0.0141 \pm 0.01	0.0234 \pm 0.02	37.12 \pm 4.01	0.9809 \pm 0.01	0.0057 \pm 0.00	0.0135 \pm 0.01
SwinMR [36]	32.89 \pm 3.42	0.9420 \pm 0.02	0.0155 \pm 0.01	0.0172 \pm 0.01	35.73 \pm 3.28	0.9590 \pm 0.02	0.0080 \pm 0.00	0.0085 \pm 0.01
RefineGAN [57]	36.36 \pm 4.01	0.9703 \pm 0.02	0.0109 \pm 0.01	0.0073 \pm 0.01	44.80 \pm 3.91	0.9910 \pm 0.01	0.0017 \pm 0.00	0.0012 \pm 0.00
SwinGAN [58]	37.44 \pm 3.34	0.9800 \pm 0.02	0.0056 \pm 0.01	0.0067 \pm 0.01	45.67 \pm 4.43	0.9954 \pm 0.00	0.0009 \pm 0.00	0.0010 \pm 0.00
OCUCFormer [59]	39.48 \pm 3.22	0.9860 \pm 0.02	0.0034 \pm 0.01	0.0065 \pm 0.02	46.78 \pm 4.40	0.9877 \pm 0.02	0.0010 \pm 0.01	0.0009 \pm 0.01
Ours	40.61\pm4.12	0.9888\pm0.01	0.0029\pm0.00	0.0056\pm0.00	47.83\pm4.18	0.9973\pm0.00	0.0006\pm0.00	0.0008\pm0.00

largest open-source MRI dataset with raw fully sampled k-space data, which includes a single-coil knee dataset and a multi-coil brain dataset. The single-coil knee dataset which consists of 973 training volumes (29877 2D slices) and 199 validation volumes (6140 2D slices) is employed in the experiments to demonstrate the effectiveness of our IGKR-Net.

IXI dataset The IXI dataset consists of 574 brain MRI volumes from normal and healthy subjects collected from three different hospitals in London. After pre-processing, 46226 2D slices from 368 volumes are used for training, 11562 2D slices from 92 volumes are used for validation, and 14315 2D slices from 114 volumes are used for testing. Since the IXI dataset does not contain the original k-space data, we use the Fast Fourier Transform (FFT) to obtain the simulated k-space data.

2) *k-space undersampling*: For these datasets, two different types of masks are tested, i.e., 1D Cartesian undersampling mask and 2D Gaussian undersampling mask. For each sampling, 20% and 40% undersampling rates are tested. Following [26], all undersampling masks are generated by first including some number of adjacent lowest frequency k-space lines or points to provide a fully-sampled k-space region. Specifically, for the 1D Cartesian undersampling mask, the fully-sampled central region includes 8% of all k-space lines; for the 2D Gaussian undersampling mask, 16% of all k-space points are included. Then, the remaining k-space lines (for 1D Cartesian mask) or points (for 2D Gaussian mask) are included uniformly at random, with the probability set so that, on average, the undersampling mask achieves the desired acceleration factor.

3) *Baselines and Training Details*: We implement our model in PyTorch using Adam with an initial learning rate of $1e-3$ and train it on 1 NVIDIA A100 GPU with 40GB

of memory. The number of epochs (E_0, E_1, E_2, E_3, E_4) for multi-stage training are set as (0, 20, 60, 100, 200).

We compare our model with the following algorithms. Zero-Filling (ZF); ResNet [56], which is trained using Adam with a learning rate of $1e-3$; the end-to-end architecture, UNet [26], provided by fastMRI, which is retrained using Adam with a learning rate of $1e-3$; RefineGAN [57], a deep learning-based generative adversarial model, which is retrained using its default parameter settings; SwinMR [36], a swin transformer based method, which is trained for 100,000 steps using Adam optimizer and the initial learning rate is set to $2e-4$ and decayed by 0.5 every 10,000 steps from the 50,000th step; SwinGAN [58], which combines the swin transformer and generative adversarial network and is retrained using its default settings; OCUCFormer [59], an over-complete under-complete transformer network, which is trained using the Adam optimizer with an initial learning rate of $1e-3$.

For the quantitative study, Peak Signal-to-Noise Ratio (PSNR), Structural Similarity Index Measure (SSIM), Normalized Mean Squared Error (NMSE), and Learned Perceptual Image Patch Similarity (LPIPS) are utilized for evaluation.

B. Experimental Results

1) *Comparisons with other methods*: In this section, we compare the performance of our IGKR-Net with other methods under different sampling patterns and acceleration rates on three public datasets.

The quantitative results of comparisons on different datasets are shown in Table I, Table II, and Table III, respectively. The best result in each column is highlighted in bold. Based on these results, we can find that: (1) Accelerated sampling leads to zero-filled MRI images with extremely poor quality; (2)

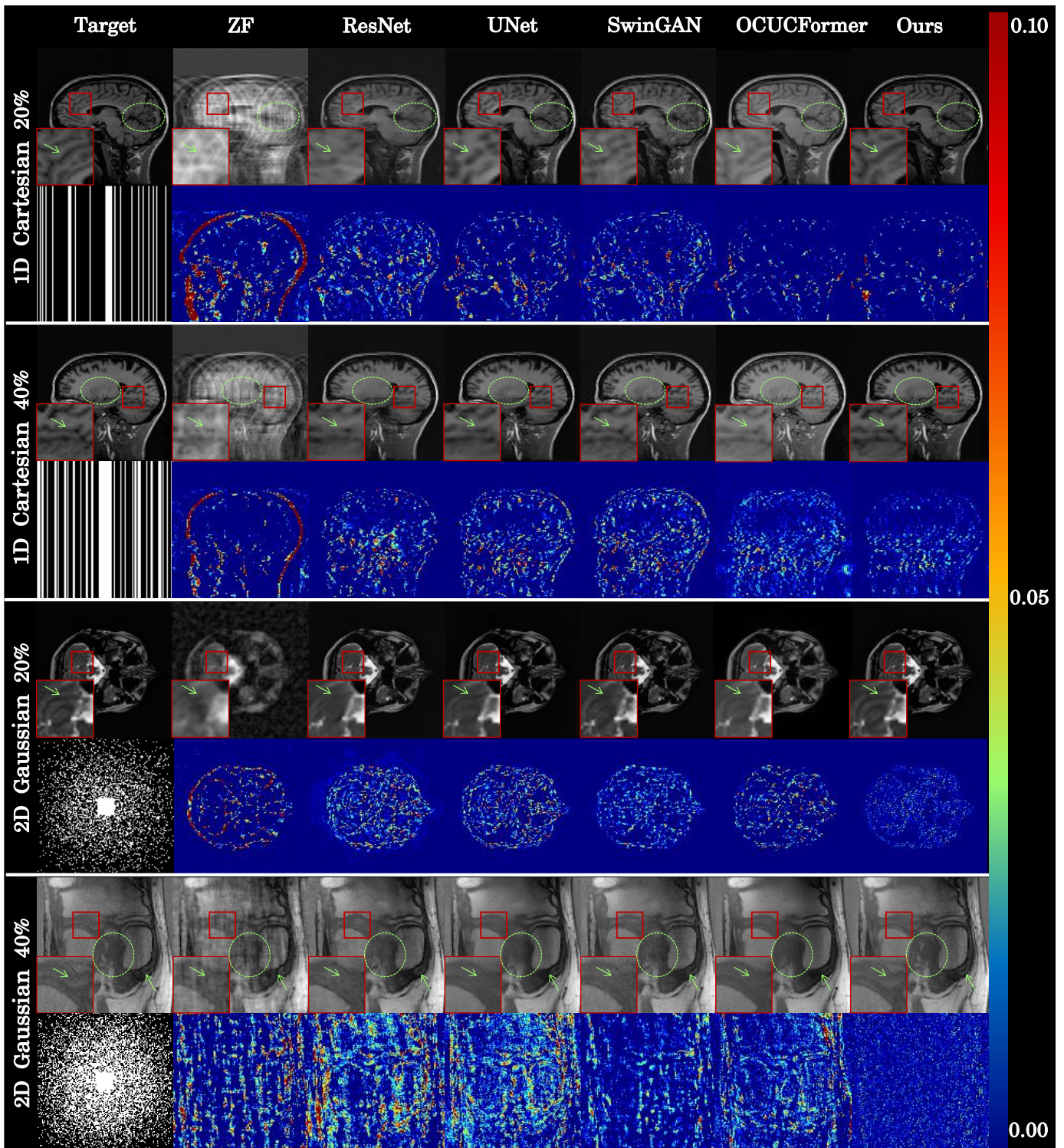


Fig. 4. Visual comparison of different methods under different masks. Red boxes illustrate the enlarged views in detail. Green ellipses and arrows highlight the performance differences in the reconstruction of anatomical structures among various methods.

Classical deep learning methods, such as UNet and ResNet, reduce image artifacts to some extent, but the restoration results remain suboptimal; (3) Current state-of-the-art methods, such as RefineGAN, SwinMR, and OCUCFormer, have significantly improved image reconstruction quality, but their performance degrades on challenging tasks with high acceleration rates (sampling rate = 20%). (4) Our method consistently

achieves the best performance with significant improvements on all datasets under different sampling scenarios. For example, as shown in Table I, our method shows the superiority of 1.54 dB and 2.63 dB in PSNR over OCUCFormer under 20% and 40% 2D random sampling masks on the CC359 dataset, respectively. As shown in Table III, our model outperforms OCUCFormer by 0.43 dB and 0.22 dB in PSNR under 20%

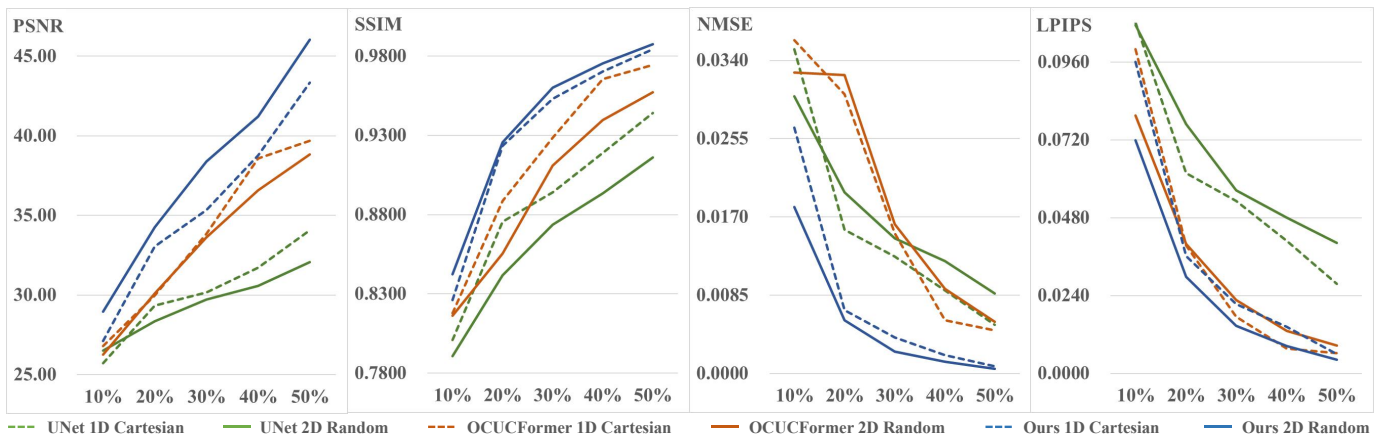


Fig. 5. Results of the experiments under masks on CC359 dataset. The X-axis represents the sampling ratio, while the Y-axis corresponds to various metrics.

TABLE IV
QUANTITATIVE RESULTS OF THE EXPERIMENTS ON DIFFERENT MASKS.

Mask type		1D Cartesian				2D Random			
ratio	Method	PSNR \uparrow	SSIM \uparrow	NMSE \downarrow	LPIPS \downarrow	PSNR \uparrow	SSIM \uparrow	NMSE \downarrow	LPIPS \downarrow
10%	UNet	25.72	0.8010	0.0352	0.1082	26.50	0.7909	0.0301	0.1075
	OCUCFormer	20.80	0.5677	0.3890	0.2839	26.27	0.7363	0.0327	0.0795
	Ours	27.11	0.8262	0.0267	0.0960	28.96	0.8424	0.0181	0.0719
20%	UNet	29.34	0.8756	0.0156	0.0618	28.34	0.8417	0.0197	0.0769
	OCUCFormer	29.96	0.8888	0.0303	0.0395	30.10	0.8554	0.0324	0.0399
	Ours	33.06	0.9234	0.0069	0.0362	34.26	0.9258	0.0058	0.0298
30%	UNet	30.15	0.8940	0.0127	0.0532	29.73	0.8738	0.0147	0.0564
	OCUCFormer	33.84	0.9286	0.0152	0.0174	33.62	0.9110	0.0162	0.0226
	Ours	35.35	0.9530	0.0039	0.0213	38.38	0.9600	0.0024	0.0147
40%	UNet	31.73	0.9189	0.0090	0.0408	30.59	0.8935	0.0122	0.0481
	OCUCFormer	38.57	0.9656	0.0058	0.0077	36.58	0.9396	0.0092	0.0131
	Ours	38.78	0.9703	0.0020	0.0143	41.22	0.9753	0.0013	0.0085
50%	UNet	34.08	0.9442	0.0053	0.0276	32.06	0.9160	0.0087	0.0402
	OCUCFormer	39.68	0.9746	0.0047	0.0063	38.84	0.9571	0.0056	0.0086
	Ours	43.34	0.9844	0.0008	0.0060	46.04	0.9875	0.0005	0.0042

and 40% 1D random masks on the IXI dataset, respectively.

The qualitative comparison results are shown in Fig.2, including the reconstructed MRI images and absolute differences (10 \times) of standardized pixel intensities between reconstructed results and Ground Truth (GT) of different methods under various masks. As observed, reconstruction using zero-filling (ZF) at high acceleration rates leads to significant aliasing artifacts and loss of anatomical details. In comparison to ZF, deep learning methods based on CNNs such as ResNet and UNet show improvement in reconstruction but still suffer from severe edge blurring and substantial detail loss. SwinGAN and OCUCFormer partially alleviate these issues, yet in challenging tasks with high acceleration rates, these methods lose some crucial anatomical details. In contrast, our IGKR-Net demonstrates robustness to sampling patterns and acceleration rates. Leveraging information from the image domain to guide the recovery in k-space, our method better preserves important anatomical details, as indicated by the arrows and ellipses.

2) *Experiments on masks*: This experimental study aims to evaluate the performance of IGKR-Net using different

TABLE V
QUANTITATIVE RESULTS OF THE ABLATION STUDIES AND ANALYSIS USING DIFFERENT MASKS ON THE CC359 VALIDATION DATASET.

Method	1D Cartesian, ratio = 20%				1D Cartesian, ratio = 40%			
	PSNR \uparrow	SSIM \uparrow	NMSE \downarrow	LPIPS \downarrow	PSNR \uparrow	SSIM \uparrow	NMSE \downarrow	LPIPS \downarrow
W/O DIFM	30.42	0.8826	0.0120	0.0612	33.67	0.9342	0.0056	0.0373
W/O TARM	31.97	0.9091	0.0086	0.0440	37.25	0.9634	0.0026	0.0186
ours	33.06	0.9234	0.0069	0.0362	38.78	0.9703	0.0020	0.0143
	2D Gaussian, ratio = 20%				2D Gaussian, ratio = 40%			
W/O DIFM	32.31	0.8838	0.0079	0.0733	37.34	0.9494	0.0025	0.0291
W/O TARM	36.11	0.9394	0.0036	0.0262	42.36	0.9788	0.0009	0.0058
Ours	37.09	0.9512	0.0029	0.0184	43.04	0.9807	0.0008	0.0048

undersampling trajectories. Five 1D Cartesian undersampling trajectories including 1D Cartesian 10%, 1D Cartesian 20%, 1D Cartesian 30%, 1D Cartesian 40% , and 1D Cartesian 50%, as well as five 2D Random undersampling trajectories including 2D Random 10%, 2D Random 20%, 2D Random 30%, 2D Random 40%, and 2D Random 50% are applied in this experiment. This experiment compares the SSIM, PSNR, NMSE, and LPIPS of UNet, OCUCFormer, and our IGKR-Net, and is conducted using the CC359 dataset.

The quantitative results of the experiment on different masks are shown in Table IV and Fig. 5, respectively. According to the results, we find that: (1) As shown in Table IV, when using the same type of mask, e.g., 1D Cartesian mask, our IGKR-Net consistently demonstrates significant improvements across different sampling rates compared to other methods. For example, our model outperforms refineGAN by 3.66 dB and 0.21 dB under 1D Cartesian mask at 50% and 40% sampling rates, respectively. (2) As shown in Fig.5, our method's performance under 2D masks (denoted as solid lines) even consistently surpasses that of other methods under 1D masks (denoted as dashed lines) in various metrics across different sampling rates, despite 1D mask being recognized as a simpler task. (3) OCUCFormer achieves satisfactory results at higher sampling rates, while its performance significantly declines under more challenging lower rates. This indicates that this method is less suitable for challenging tasks while our method shows robustness across various masks.

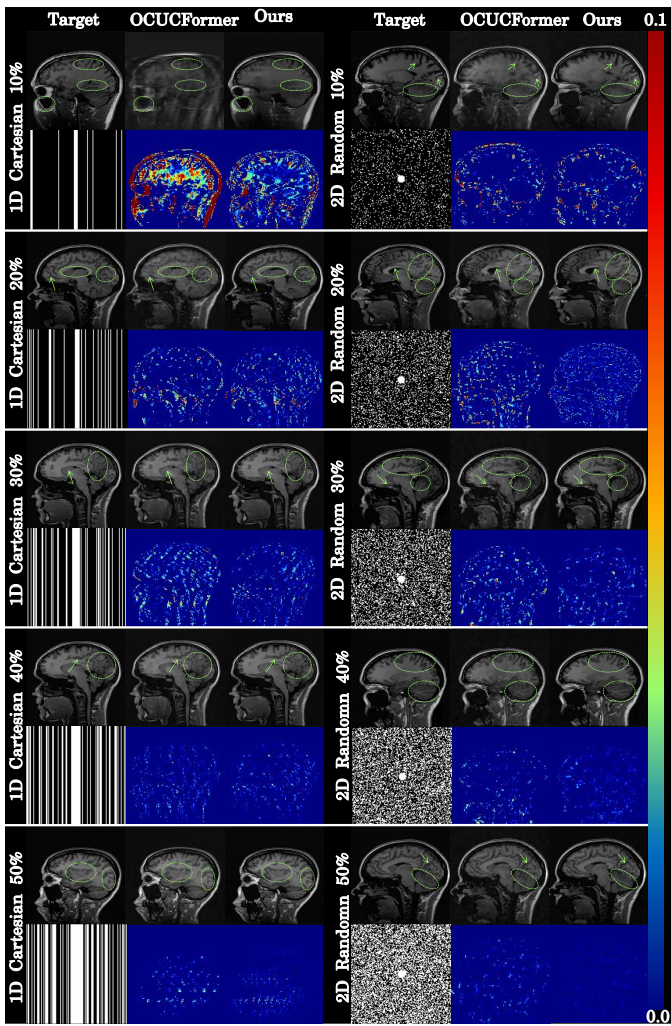


Fig. 6. Visual comparison of the experiment under different masks.

The sample of reconstructed images and absolute differences of standardized pixel intensities ($10\times$) between reconstructed images and GT are shown in Fig.6. According to the results, it can be observed that as the k-space sampling ratio increases, the performance of different methods steadily improves. It is noteworthy that in challenging tasks with low sampling rates, e.g., 1D or 2D 10%, other methods obtain extremely poor performance, while our method can still reconstruct relatively clear contour edges. Overall, our IGKR-Net achieved a higher reconstruction quality compared to other methods under various undersampling trajectories.

C. Ablation Studies and Analysis

1) *Efficacy of Key Components*: To validate the effectiveness of our proposed Image Domain Guidance Module (IDGM) and Tri-Attention Refinement Module (TARM), ablation experiments are conducted on these two modules. Specifically, we design two network variants: (1) w/o DIFM, in which the DIFM module is removed from the network and the k-space spectrum outputted from the LRIT is directly used for HRIT; (2) w/o TARM, the TARM module is removed from the network and the MRI image outputted from the HRIT is regarded as final reconstruction result.

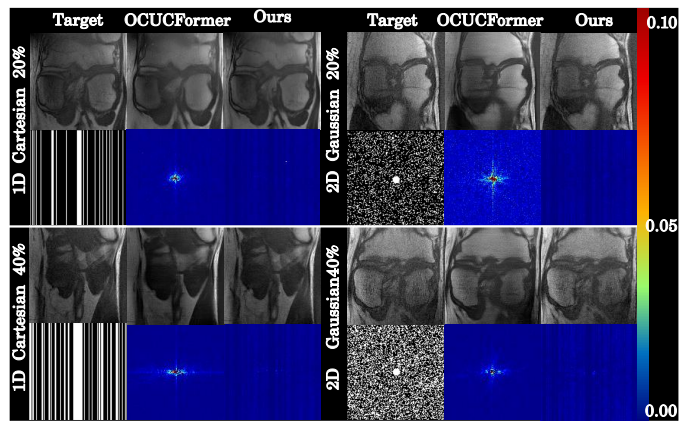


Fig. 7. Visual comparison with k-space error maps under different masks.

The performance of the above variant networks is tested by using different masks on the CC359 dataset, and the experimental results are shown in Table V. It can be observed that after removing the TARM module, the performance decreased significantly, which verifies that our proposed TARM can better refine the output and thus guide MRI image reconstruction. In addition, the W/O IDGM network variant achieves the poorest results, which demonstrates that our proposed IDGM module can mine semantic information from undersampled MRI images to obtain more informative outputs.

2) *Efficacy of recovering k-space*: To further analyze the effectiveness of our approach in the recovery of k-space, we present the results of k-space reconstruction, as shown in Fig. 7. Specifically, we show the sample of reconstructed images and absolute differences ($10\times$) of standardized pixel intensities between reconstructed k-space and GT ones. It can be observed that our method achieves a generally low error in the recovered spectrum. Corresponding to the MRI images, it is evident that our approach excels in recovering high-frequency details and edges, while other methods tend to exhibit issues of over-smoothing. This further substantiates the importance of k-space recovery for the precise reconstruction of MRI images and the effectiveness of our proposed method.

V. CONCLUSION

In this paper, we focused on the problem of image-domain guided k-space recovery for MRI reconstruction. We proposed a novel method, called IGKR-Net, which tackled the key problem of current deep learning based MRI reconstruction methods, namely the insufficient and unsuitable k-space recovery. Specifically, an implicit transformer based k-space reconstruction is proposed to efficiently learn continuous feature space and recover high-quality k-space in the Fourier domain. This mechanism facilitates more precise and effective learning of continuous representations of k-space information, resulting in precise k-space spectrum that are more favorable for MRI reconstruction. Furthermore, an image domain enhancement branch consists of a fusion module and a refinement module is introduced to enable accurate dual-domain feature aggregation and image refinement, thereby guiding MRI reconstruction. Our method demonstrates superior performance on publicly available datasets, confirming its effectiveness.

REFERENCES

- [1] A. L. Scherzinger and W. R. Hendee, "Basic principles of magnetic resonance imaging—an update," *Western journal of medicine*, vol. 143, no. 6, p. 782, 1985.
- [2] M. Doneva, "Mathematical models for magnetic resonance imaging reconstruction: An overview of the approaches, problems, and future research areas," *IEEE Signal Processing Magazine*, vol. 37, no. 1, pp. 24–32, 2020.
- [3] M. Lustig, D. Donoho, and J. M. Pauly, "Sparse mri: The application of compressed sensing for rapid mr imaging," *Magnetic Resonance in Medicine: An Official Journal of the International Society for Magnetic Resonance in Medicine*, vol. 58, no. 6, pp. 1182–1195, 2007.
- [4] U. Gamber, P. Boesiger, and S. Kozerke, "Compressed sensing in dynamic mri," *Magnetic Resonance in Medicine: An Official Journal of the International Society for Magnetic Resonance in Medicine*, vol. 59, no. 2, pp. 365–373, 2008.
- [5] K. P. Pruessmann, M. Weiger, M. B. Scheidegger, and P. Boesiger, "Sense: sensitivity encoding for fast mri," *Magnetic Resonance in Medicine: An Official Journal of the International Society for Magnetic Resonance in Medicine*, vol. 42, no. 5, pp. 952–962, 1999.
- [6] S. Wang, Z. Su, L. Ying, X. Peng, S. Zhu, and F. Liang, "Accelerating magnetic resonance imaging via deep learning," in *2016 IEEE 13th international symposium on biomedical imaging (ISBI)*. IEEE, 2016, pp. 514–517.
- [7] Y. Yang, J. Sun, H. Li, and Z. X. ADMM-Net, "A deep learning approach for compressive sensing mri," *CoRR*, abs/1705.06869, 2017b. URL <http://arxiv.org/abs/1705.06869>, 2017.
- [8] K. Hammernik, T. Klatzer, E. Kobler, M. P. Recht, D. K. Sodickson, T. Pock, and F. Knoll, "Learning a variational network for reconstruction of accelerated mri data," *Magnetic resonance in medicine*, vol. 79, no. 6, pp. 3055–3071, 2018.
- [9] K. H. Jin, M. T. McCann, E. Froustey, and Unser, "Deep convolutional neural network for inverse problems in imaging," *IEEE transactions on image processing*, vol. 26, no. 9, pp. 4509–4522, 2017.
- [10] K. Hammernik, T. Küstner, B. Yaman, Z. Huang, D. Rueckert, F. Knoll, and et al, "Physics-driven deep learning for computational magnetic resonance imaging: Combining physics and machine learning for improved medical imaging," *IEEE Signal Processing Magazine*, vol. 40, no. 1, pp. 98–114, 2023.
- [11] C. M. Hyun, H. P. Kim, S. M. Lee, S. Lee, and J. K. Seo, "Deep learning for undersampled mri reconstruction," *Physics in Medicine & Biology*, vol. 63, no. 13, p. 135007, 2018.
- [12] G. Yang, S. Yu, H. Dong, G. Slabaugh, P. L. Dragotti, X. Ye, and et al, "Dagan: Deep de-aliasing generative adversarial networks for fast compressed sensing mri reconstruction," *IEEE transactions on medical imaging*, vol. 37, no. 6, pp. 1310–1321, 2017.
- [13] C. Qin, J. Schlemper, J. Caballero, A. N. Price, J. V. Hajnal, and D. Rueckert, "Convolutional recurrent neural networks for dynamic mr image reconstruction," *IEEE Transactions on Medical Imaging*, vol. 38, no. 1, pp. 280–290, 2019.
- [14] Y. Han and L. Sunwoo, "k-space deep learning for accelerated mri," *IEEE transactions on medical imaging*, vol. 39, no. 2, pp. 377–386, 2019.
- [15] A. Sriram, J. Zbontar, T. Murrell, C. L. Zitnick, A. Defazio, and et al, "Grappanet: Combining parallel imaging with deep learning for multi-coil mri reconstruction," in *2020 IEEE/CVF Conference on Computer Vision and Pattern Recognition (CVPR)*, 2020, pp. 14 303–14 310.
- [16] L. Sun, Y. Wu, B. Shu, X. Ding, C. Cai, Y. Huang, and J. Paisley, "A dual-domain deep lattice network for rapid mri reconstruction," *Neurocomputing*, vol. 397, pp. 94–107, 2020.
- [17] X. Liu, Y. Pang, R. Jin, Y. Liu, and Z. Wang, "Dual-domain reconstruction network with v-net and k-net for fast mri," *Magnetic Resonance in Medicine*, vol. 88, no. 6, pp. 2694–2708, 2022.
- [18] H. Wang, X. Hu, X. Zhao, and Y. Zhang, "Wide weighted attention multi-scale network for accurate mr image super-resolution," *IEEE Transactions on Circuits and Systems for Video Technology*, vol. 32, no. 3, pp. 962–975, 2022.
- [19] K. Möllenhoff, A.-M. Oros-Peusquens, and N. J. Shah, "Introduction to the basics of magnetic resonance imaging," *Molecular Imaging in the Clinical Neurosciences*, pp. 75–98, 2012.
- [20] A. S. Minhas and R. Oliver, "Magnetic resonance imaging basics," *Electrical Properties of Tissues: Quantitative Magnetic Resonance Mapping*, pp. 47–82, 2022.
- [21] R. Mulkern and T. Chung, "From signal to image: magnetic resonance imaging physics for cardiac magnetic resonance," *Pediatric cardiology*, vol. 21, pp. 5–17, 2000.
- [22] M. M. Moore and T. Chung, "Review of key concepts in magnetic resonance physics," *Pediatric radiology*, vol. 47, pp. 497–506, 2017.
- [23] Y. Chen, S. Liu, and X. Wang, "Learning continuous image representation with local implicit image function," in *Proceedings of the IEEE/CVF conference on computer vision and pattern recognition*, 2021, pp. 8628–8638.
- [24] X. Xu, Z. Wang, and H. Shi, "Ultrasr: Spatial encoding is a missing key for implicit image function-based arbitrary-scale super-resolution," *arXiv preprint arXiv:2103.12716*, 2021.
- [25] H. Li, T. Dai, Y. Li, X. Zou, and S.-T. Xia, "Adaptive local implicit image function for arbitrary-scale super-resolution," in *2022 IEEE International Conference on Image Processing (ICIP)*. IEEE, 2022, pp. 4033–4037.
- [26] J. Zbontar, F. Knoll, A. Sriram, T. Murrell, Z. Huang, and M. J. Muckley, "fastmri: An open dataset and benchmarks for accelerated mri," *arXiv preprint arXiv:1811.08839*, 2018.
- [27] D. Lee, J. Yoo, S. Tak, and J. C. Ye, "Deep residual learning for accelerated mri using magnitude and phase networks," *IEEE Transactions on Biomedical Engineering*, vol. 65, no. 9, pp. 1985–1995, 2018.
- [28] M. Mardani, E. Gong, J. Y. Cheng, S. S. Vasanawala, G. Zaharchuk, L. Xing, and et al, "Deep generative adversarial neural networks for compressive sensing mri," *IEEE Transactions on Medical Imaging*, vol. 38, no. 1, pp. 167–179, 2019.
- [29] Jo, Schlemper, Jose, Caballero, Joseph, Hajnal, and et al, "A deep cascade of convolutional neural networks for dynamic mr image reconstruction," *IEEE Transactions on Medical Imaging*, 2017.
- [30] Z. Yang, K. Fu, M. Duan, L. Qu, S. Wang, and Z. Song, "Separate and conquer: Decoupling co-occurrence via decomposition and representation for weakly supervised semantic segmentation," in *Proceedings of the IEEE/CVF Conference on Computer Vision and Pattern Recognition (CVPR)*, June 2024, pp. 3606–3615.
- [31] Z. Yang, Y. Meng, K. Fu, S. Wang, and Z. Song, "Tackling ambiguity from perspective of uncertainty inference and affinity diversification for weakly supervised semantic segmentation," 2024. [Online]. Available: <https://arxiv.org/abs/2404.08195>
- [32] T. Gao, Y. Wen, K. Zhang, J. Zhang, T. Chen, L. Liu, and W. Luo, "Frequency-oriented efficient transformer for all-in-one weather-degraded image restoration," *IEEE Transactions on Circuits and Systems for Video Technology*, vol. 34, no. 3, pp. 1886–1899, 2024.
- [33] X. Feng, H. Ji, W. Pei, J. Li, G. Lu, and D. Zhang, "U²-former: Nested u-shaped transformer for image restoration via multi-view contrastive learning," *IEEE Transactions on Circuits and Systems for Video Technology*, vol. 34, no. 1, pp. 168–181, 2024.
- [34] C.-M. Feng, Y. Yan, H. Fu, and Y. Xu, "Task transformer network for joint mri reconstruction and super-resolution," in *Medical Image Computing and Computer Assisted Intervention—MICCAI 2021: 24th International Conference, Strasbourg, France, September 27–October 1, 2021, Proceedings, Part VI 24*. Springer, 2021, pp. 307–317.
- [35] C.-M. Feng, Y. Yan, G. Chen, Y. Xu, Y. Hu, L. Shao, and et al, "Multi-modal transformer for accelerated mr imaging," *IEEE Transactions on Medical Imaging*, 2022.
- [36] J. Huang, Y. Fang, Y. Wu, H. Wu, Z. Gao, Y. Li, and et al, "Swin transformer for fast mri," *Neurocomputing*, vol. 493, pp. 281–304, 2022.
- [37] V. S. Vassiliou, D. Cameron, S. K. Prasad, and P. D. Gatehouse, "Magnetic resonance imaging: Physics basics for the cardiologist," *JRSM cardiovascular disease*, vol. 7, p. 2048004018772237, 2018.
- [38] S. Ravishanker and Y. Bresler, "Mr image reconstruction from highly undersampled k-space data by dictionary learning," *IEEE Transactions on Medical Imaging*, vol. 30, no. 5, pp. 1028–1041, 2011.
- [39] T. Eo, Y. Jun, T. Kim, J. Jang, H.-J. Lee, and D. Hwang, "Kiki-net: cross-domain convolutional neural networks for reconstructing undersampled magnetic resonance images," *Magnetic resonance in medicine*, vol. 80, no. 5, pp. 2188–2201, 2018.
- [40] O. Nitski, S. Nag, C. McIntosh, and B. Wang, "Cdf-net: Cross-domain fusion network for accelerated mri reconstruction," in *Medical Image Computing and Computer Assisted Intervention – MICCAI 2020*, A. L. Martel, P. Abolmaesumi, D. Stoyanov, D. Mateus, M. A. Zuluaga, S. K. Zhou, D. Racoceanu, and L. Joskowicz, Eds. Cham: Springer International Publishing, 2020, pp. 421–430.
- [41] Z. Wang, M. Ran, Z. Yang, H. Yu, J. Jin, T. Wang, J. Lu, and Y. Zhang, "Generalizable mri motion correction via compressed sensing equivariant imaging prior," *IEEE Transactions on Circuits and Systems for Video Technology*, pp. 1–1, 2024.
- [42] X. Zhao, T. Yang, and X. Zhang, "Swingan: A dual-domain swin transformer-based generative adversarial network for mri reconstruction," *Computers in Biology and Medicine*, vol. 153, no. 5, p. 106513, 2023.

- [43] M. A. Griswold, P. M. Jakob, R. M. Heidemann, M. Nittka, V. Jellus, J. Wang, B. Kiefer, and A. Haase, "Generalized autocalibrating partially parallel acquisitions (grappa)." *Magnetic resonance in medicine*, vol. 47, no. 6, p. 1202, 2002.
- [44] M. Lustig and J. M. Pauly, "Spirit: iterative self-consistent parallel imaging reconstruction from arbitrary k-space," *Magnetic resonance in medicine*, vol. 64, no. 2, pp. 457–471, 2010.
- [45] J. P. Haldar, "Autocalibrated loraks for fast constrained mri reconstruction," in *2015 IEEE 12th International Symposium on Biomedical Imaging (ISBI)*.
- [46] M. Akçakaya, S. Moeller, S. Weingärtner, and K. Uğurbil, "Scan-specific robust artificial-neural-networks for k-space interpolation (raki) reconstruction: Database-free deep learning for fast imaging," *Magnetic resonance in medicine*, vol. 81, no. 1, pp. 439–453, 2019.
- [47] V. Sitzmann, J. Martel, A. Bergman, D. Lindell, and G. Wetzstein, "Implicit neural representations with periodic activation functions," *Advances in neural information processing systems*, vol. 33, pp. 7462–7473, 2020.
- [48] D. Grattarola and P. Vandergheynst, "Generalised implicit neural representations," *Advances in Neural Information Processing Systems*, vol. 35, pp. 30 446–30 458, 2022.
- [49] Z. Chen, Y. Chen, J. Liu, X. Xu, V. Goel, Z. Wang, and X. Wang, "Videoir: Learning video implicit neural representation for continuous space-time super-resolution," in *Proceedings of the IEEE/CVF Conference on Computer Vision and Pattern Recognition (CVPR)*, June 2022, pp. 2047–2057.
- [50] Z. Chen and H. Zhang, "Learning implicit fields for generative shape modeling," in *Proceedings of the IEEE/CVF Conference on Computer Vision and Pattern Recognition*, 2019, pp. 5939–5948.
- [51] B. Mildenhall, P. P. Srinivasan, M. Tancik, J. T. Barron, R. Ramamoorthi, and R. Ng, "Nerf: Representing scenes as neural radiance fields for view synthesis," *Communications of the ACM*, vol. 65, no. 1, pp. 99–106, 2021.
- [52] N. Rahaman, A. Baratin, D. Arpit, F. Draxler, M. Lin, F. Hamprecht, Y. Bengio, and A. Courville, "On the spectral bias of neural networks," in *International Conference on Machine Learning*. PMLR, 2019, pp. 5301–5310.
- [53] X. Zheng, Z. Li, D. Liu, X. Zhou, and C. Shan, "Spatial attention-guided light field salient object detection network with implicit neural representation," *IEEE Transactions on Circuits and Systems for Video Technology*, pp. 1–1, 2024.
- [54] H. Chen, W. Zhao, T. Xu, G. Shi, S. Zhou, P. Liu, and J. Li, "Spectral-wise implicit neural representation for hyperspectral image reconstruction," *IEEE Transactions on Circuits and Systems for Video Technology*, vol. 34, no. 5, pp. 3714–3727, 2024.
- [55] Q. Wu, Y. Li, Y. Sun, Y. Zhou, and H. Wei, "An arbitrary scale super-resolution approach for 3d mr images via implicit neural representation," *IEEE Journal of Biomedical and Health Informatics*, 2022.
- [56] K. He, X. Zhang, and J. Sun, "Deep residual learning for image recognition," in *Proceedings of the IEEE conference on computer vision and pattern recognition*, 2016, pp. 770–778.
- [57] T. M. Quan and W.-K. Jeong, "Compressed sensing mri reconstruction using a generative adversarial network with a cyclic loss," *IEEE transactions on medical imaging*, vol. 37, no. 6, pp. 1488–1497, 2018.
- [58] X. Zhao, T. Yang, B. Li, and X. Zhang, "Swingan: A dual-domain swin transformer-based generative adversarial network for mri reconstruction," *Computers in Biology and Medicine*, vol. 153, p. 106513, 2023. [Online]. Available: <https://www.sciencedirect.com/science/article/pii/S0010482522012215>
- [59] M. A. Fahim, S. Ramanarayanan, G. Rahul, M. N. Gayathri, A. Sarkar, K. Ram, and M. Sivaprakasam, "Ocuformer: An over-complete under-complete transformer network for accelerated mri reconstruction," *Image and Vision Computing*, vol. 150, p. 105228, 2024. [Online]. Available: <https://www.sciencedirect.com/science/article/pii/S0262885624003330>
- [60] B. Zhou and S. K. Zhou, "Dudornet: Learning a dual-domain recurrent network for fast mri reconstruction with deep t1 prior," in *2020 IEEE/CVF Conference on Computer Vision and Pattern Recognition (CVPR)*, 2020, pp. 4272–4281.